Spectrochimica Acta Part A: Molecular and Biomolecular Spectroscopy 320 (2024) 124616

Contents lists available at ScienceDirect

Spectrochimica Acta Part A:
Molecular and Biomolecular Spectroscopy

journal homepage: www.journals.elsevier.com/spectrochimica-acta-part-a-molecular-and-biomolecular-spectroscopy

Exploring microstructures of metal-doped oxides via simulated Raman spectrum

Le Liu [a,1], Yuxing Xu [b,1], Junchao Su [a], Jiangtao Wei [a], Xingchen Liu [c], Qing Peng [d,*], Jie Chang [e,*], Botao Teng [a,*]

[a] Tianjin Key Laboratory of Brine Chemical Engineering and Resource Eco-utilization, College of Chemical Engineering and Materials Science, Tianjin University of Science and Technology, Tianjin 300457, China
[b] Department of Chemical Physics, University of Science and Technology of China, Hefei 230026, China
[c] State Key Laboratory of Coal Conversion, Institute of Coal Chemistry, Chinese Academy of Sciences, Taiyuan 030001, China
[d] State Key Laboratory of Nonlinear Mechanics, Institute of Mechanics, Chinese Academy of Sciences, Beijing 100190, China
[e] Institute of Sustainability of Chemical, Energy and Environment, Agency for Science, Technology and Research, Singapore 627833, Singapore

HIGHLIGHTS

- Global searching, Boltzmann distribution and Raman simulation was integrated.
- Weighted Raman spectra of Zr-doped ceria was used as a demonstration.
- It is also validated for analysis of microstructure of metal composite oxides.
- This provides a solution to explore the microstructure of composites.

GRAPHICAL ABSTRACT

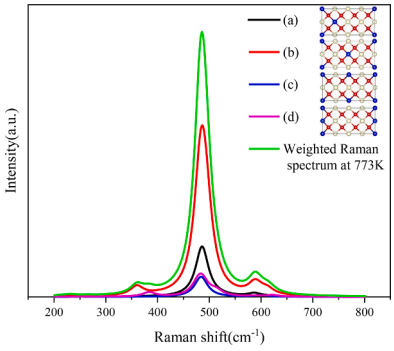

ARTICLE INFO

Keywords:
Metal-doped oxide
Global structure searching
Boltzmann distribution
Simulated Raman spectrum
$Ce_{1-x}Zr_xO_2$
Microstructure

ABSTRACT

Solid solution of metal-doped oxide has been widely used in material industry and catalysis process. Its performance is highly correlated with the distribution of doped ions. Due to the complex distribution of doped ions in solid solution and its variation with temperatures, to obtain the microstructures of metal-doped ions in solid solution remains a substantial challenge. Taken $Ce_{1-x}Zr_xO_2$ as a model, the global structure searching, structures proportion with temperature determined by Boltzmann distribution, and the weighted simulation Raman spectra were integrated to explore the microstructures of metal-doped solid solution oxides. It was further verified by application into rutile and anatase TiO_2 mixture, indicating that the present method is feasible to deduce the microstructure of metal composite oxides. We anticipate that it provides a powerful solution to explore microstructures of solid solution and complex metal oxides.

* Corresponding authors.
E-mail addresses: pengqing@imech.ac.cn (Q. Peng), Chang_jie@isce2.a-star.edu.sg (J. Chang), tbt@zjnu.cn (B. Teng).
[1] L. Liu and Y. Xu contributed equally.

https://doi.org/10.1016/j.saa.2024.124616
Received 22 November 2023; Received in revised form 30 May 2024; Accepted 5 June 2024
Available online 6 June 2024

1. Introduction

Solid solution of metal-doped oxide is a very important kind of metal composite oxides and has been widely used in material industry and catalysis process [1–5]. By introducing the doped ions to form new chemical bonds, the thermal and chemical stability, as well as performances could be enhanced [6–8]. For example, Li et al. [9] studied the iron-doped ceria and found that Ce-Fe-O solid solution forms when the concentration of iron ion is less than 0.3; while Fe_2O_3 appears with further increase of the concentration of Fe ion with higher activity in CH_4 oxidation. Sartoretti et al. [10] investigated Cu and Mn-doped ceria and found that 5 % Cu-doped catalyst has higher surface area, but lower activity in soot oxidation; while 5 % Mn-doped ceria has the best activity in soot oxidation. Therefore, the catalytic performance of metal-doped solid solution is closely related to the type, concentration and distribution of doping ions [11].

Compared with the type and concentration of doping ions, the distribution of doped ions in solid solution also plays a key role in oxidative catalysis. It was reported that the metal-doped oxides mostly follow the Mars-van Krevelen mechanism, in which the doped ions integrate into the lattice of catalyst and lead to the geometrical stress and charge imbalance [12]. Hence, metal-doped oxides usually have lower oxygen defect formation energy and generate more oxygen vacancies than pure oxides due to the doped ion radius and charge imbalance [13]. Correspondingly, O_2 adsorbs on oxygen defects and forms active oxygen species to participate in the oxidation reaction [14]. Therefore, the catalytic performances of metal-doped oxides are highly correlated with the formation energy of oxygen defects, which in turn is closely related to the distribution of doped ions [15]. This is due to the fact that the oxygen defect formation energy in pure metal oxide only depends on the interaction between the host metal (M1) ions and oxygen atoms (M1-O-M1); while in solid solution with doped metal ion (M2), there are M1-O-M1, M1-O-M2 and M2-O-M2 interactions depending on the distribution of the doped metal ions in solid solution [16]. Therefore, exploring the corresponding distribution would improve the understanding of the microstructure of the doped solid solution and help the rational design and development of metal-doped oxides with high performance.

However, due to the complex distribution of doped ions in solid solution and variation with temperature, obtaining the microstructure information remains a substantial challenge. Among the widely used characterization techniques, X-ray diffraction (XRD) can determine whether solid solution is formed or not by measuring lattice parameters of doped solid solution [17]; X-ray photoelectronic spectroscopy (XPS) can measure the valence of elements in surface layer of materials [18]; X-ray fluorescence spectroscopy (XRF) can measure the concentration of atoms in composite oxides; UV–Vis can determine whether there are isolated doped cations; EXAFS can measure the coordination environment and structure of doped atoms [19]. Although these techniques greatly enriched our knowledge on the microstructure of metal doped solid solution, they are hard to obtain the quantitative distribution of metal-doped oxides.

Raman spectroscopy is a rapid nondestructive technology [20], which can provide important structure information by measuring the characteristic vibration of pure and doped phase [21–26]. For example, $Ce_{1-x}Zr_xO_2$ ($0 < x < 0.5$) is a typical solid solution with a high Raman peak of 485 cm^{-1}, as well as a wide and small peak of 600 cm^{-1} [27]. Using the most stable $Ce_6Zr_2O_8$ model, our simulated Raman spectrum indicated that the 485 cm^{-1} peak is contributed by F_{2g} vibration; and the wide and small one of 600 cm^{-1} is designated to Ce^{4+}-O-Zr^{4+} vibration [28]. Furthermore, the F_{2g} peak of $Ce_{1-x}Zr_xO_2$ solid solution blue shifts about 25 cm^{-1} compared with 460 cm^{-1} of CeO_2, which is derived from the relatively smaller size of Zr^{4+} ion (0.84 Å) compared with Ce^{4+} ion (0.97 Å). Although the simulated spectrum interpreted the derivation of Raman peaks of $Ce_{1-x}Zr_xO_2$ solid solution at a molecular level, the narrow peak at 600 cm^{-1} of the simulated spectrum is quite different from the small and wide peak in experimental spectrum. This might be attributed to the various Ce and Zr distributions in $Ce_{1-x}Zr_xO_2$ solid solution, which cannot be represented by the most stable structure. Therefore, it is possible to obtain a spectrum close to the experimental one if the composition of solid solution approaches the practical catalyst. Correspondingly, the Ce and Zr distribution in metal-doped oxides can be reasonably obtained by simulated Raman spectra.

To solve the challenge of the microstructures of doped ions in solid solution, using $Ce_{1-x}Zr_xO_2$ as a case, a protocol to quantitatively determine the microstructures of doped ions was proposed to get the weighted theoretical Raman spectrum in the present work based on Boltzmann statistical average of different configurations [29–31]. It was further verified by application in mixed TiO_2 by correlating the ratio of mixed oxides with the simulated Raman spectra. Therefore, it provides a feasible solution to establish the possible relationship between the material structure and Raman spectra.

2. Method and models

The present protocol includes the global searching and optimization of the possible structures of solid solution oxide, simulation of Raman spectra of different configurations, as well as calculation of the weighted theoretical Raman spectrum. For clear explanation, the solid solution of $Ce_{1-x}Zr_xO_2$ which has been widely applied in the elimination of volatile organic compounds, the three-way catalytic purification of automobile exhaust, etc., was taken as an example [32,33]. A supercell of $Ce_6Zr_2O_{16}$ was adopted to represent the $Ce_{0.75}Zr_{0.25}O_2$ solid solution, and all of its possible structures were generated by using the site-occupancy disorder (SOD) method [34], in which all the possible configurations was generated by atomic substitutions via the group of symmetry operator in parent structure. Then the structures were optimized by Vienna ab initio simulation package (VASP) [35]. Projector augmented wave (PAW) [36] pseudopotential was utilized with Perdew-Burke-Ernzerhof [37] functional and generalized gradient approximation. Monkhorst-Pack method was adopted for Brillouin zone sampling [38]. Kohn-Sham equations were solved with a cutoff energy of 400 eV. 1.0×10^{-8} eV and 0.01 eV/Å were set for the energy convergence criterion and the maximum Hellmann-Feynman force, respectively [23]. DFT + U method with U value of 5 eV for Ce atom was performed for the correction of on-site Coulombic and exchange interactions produced by strong localization of 4f electrons [39,40]. The Raman spectrum simulation includes the matrix vibration calculation phonon spectra and dielectric coefficient by density functional perturbation theory (DFPT) [41–43].

The proportion of $Ce_6Zr_2O_{16}$ with different structures in solid solution at specific temperature was calculated based on the equation of Boltzmann distribution, Eq. (1) [44].

$$\frac{N_i}{N} = \frac{g_i e^{-\frac{(\Delta\varepsilon_i+\varepsilon_{\mathrm{Ref}})}{kT}}}{\sum_i g_i e^{-\frac{(\Delta\varepsilon_i+\varepsilon_{\mathrm{Ref}})}{kT}}} = \frac{g_i e^{-\frac{\Delta\varepsilon_i}{kT}}}{\sum_i g_i e^{-\frac{\Delta\varepsilon_i}{kT}}} \tag{1}$$

where N_i is the number of ith structure; N is the total number of all structures; g_i is degeneracy of ith structure; $\varepsilon_{\mathrm{Ref}}$ is the free energy of the most stable configuration; $\Delta\varepsilon_i$ is the free energy difference of ith structure compared with $\varepsilon_{\mathrm{Ref}}$; k is Boltzmann's constant.

The weighted simulation Raman spectra was calculated according to the following equation.

$$I_{\mathrm{total}} = \sum_i \left(\frac{N_i}{N} \times I_i\right) \tag{2}$$

where I_i and I_{total} are the intensities of Raman spectra for the ith structure and the total one, respectively. N_i/N is the structural proportion of the ith configuration.

3. Results and discussion

After the global searching and optimization of the supercell of $Ce_6Zr_2O_{16}$ by SOD method and DFT calculation, four stable configurations and their simulated Raman spectra were depicted in Fig. 1; the free energies and proportion at different temperature based on the Boltzmann distribution calculation were listed in Table 1.

As listed in Table 1, Structure (a) with the biggest distance of two Zr ions is the most stable configuration and is dominant in solid solution at zero temperature. When the temperature increases to 300 K, the ratios of Structure (a)~(d) are 0.279, 0.677, 0.023 and 0.020, respectively. With further increase to 773 K, the ratios of Structure (a) and (b) decrease to 0.190 and 0.646, respectively; while the ratio of Structure (c) and (d) increase to 0.076 and 0.088, respectively. Therefore, it can be reasonably deduced that the Raman spectra of $Ce_{1-x}Zr_xO_2$ will vary with temperature.

Fig. 1 showed that the F_{2g} vibration modes of all configurations blue shift to 485 cm^{-1} compared with CeO_2 (460 cm^{-1}) due to the lattice contraction and the shortening of Ce-O bond length caused by the doping Zr ions [25]. The Raman spectra of Structure (a) and (c) are very similar since the F_{2g} peaks almost overlap, and there is only one small peak at 585 (a) and 600 cm^{-1} (c), which are assigned as Zr^{4+}-O-Ce^{4+} vibration peak. Except for the F_{2g} peak, Structure (b) has three peaks at 360, 589 and 610 cm^{-1}, which are caused by vibrations of O-Zr^{4+}-O, Zr^{4+}-O-Ce^{4+} and Zr^{4+}-O-Zr^{4+}, respectively. The Raman spectrum of Structure (d) is similar to that of Structure (b) with two small peaks at 590 and 622 cm^{-1}, respectively. The calculation results above indicated that a small and wide Raman peak may appear from 580 cm^{-1} to 630 cm^{-1} due to the coexistence of multiple microstructures of $Ce_{1-x}Zr_xO_2$ solid solution.

To verify the theoretical deduction of the weak broad peaks between 580 and 620 cm^{-1} derived from the overlap of $Ce_{1-x}Zr_xO_2$ with different Ce and Zr distribution, the weighted Raman spectra at different temperature were calculated and shown in Fig. 2. At 0 K, the Raman spectrum of $Ce_{1-x}Zr_xO_2$ is determined by the most stable Structure (a) with a F_{2g} peak of 485 cm^{-1} and a characteristic one of 586 cm^{-1}. When temperature rises to 300 K, the fractions of Structure (a)~(d) are 0.279, 0.677, 0.023 and 0.020, respectively. Hence, the weighted Raman spectrum at 300 K is mainly contributed by Structure (a) and (b). When temperature is up to 773 K, the ratios of Structure (a)~(d) are 0.190, 0.646, 0.076 and 0.088. Corresponding, the small and broad Raman peaks at 580 ~ 630 cm^{-1} are contributed by all the four structures. The small and broad peak between 585 cm^{-1} and 620 cm^{-1} are derived from vibrations of Zr^{4+}-O-Ce^{4+} and Zr^{4+}-O-Zr^{4+} of $Ce_{1-x}Zr_xO_2$ solid solution with different Ce and Zr distribution, respectively. The peak of 585 cm^{-1} is mainly caused by the Zr^{4+}-O-Ce^{4+} vibration; and the peak of 620 cm^{-1} is caused by Zr^{4+}-O-Zr^{4+} vibration. Their overlap results in the broadening of Raman peak of 580 ~ 630 cm^{-1}. Fig. 2 also indicates that the peaks at 580–630 cm^{-1} blue shift with the increase of temperature, indicating the microstructure varies with temperature.

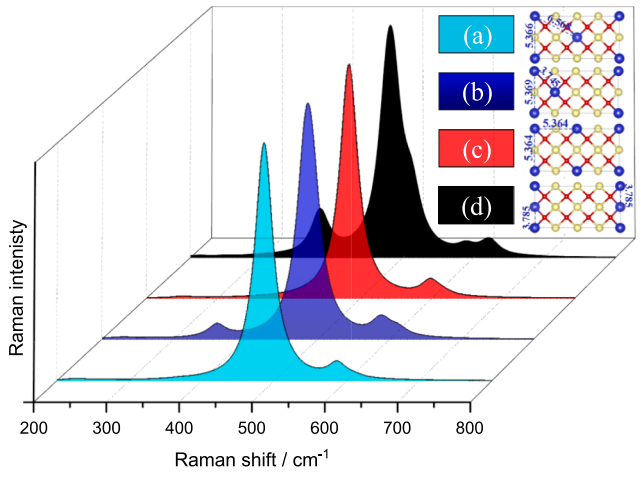

Fig. 1. Simulated Raman spectra of four $Ce_6Zr_2O_{16}$ configurations with different Zr-Zr distance.

To prove this deduction above, the $Ce_{0.75}Zr_{0.25}O_2$ samples was prepared by the citrate sol–gel method and treated with two heated approaches. One was calcined at 773 K for 4 h and slowly annealed at muffle furnace to room temperature; the other one was calcined at 773 K for 4 h and fast cooled to room temperature. As shown in Fig. 3, the inset of X-ray diffraction patterns showed that $Ce_{0.75}Zr_{0.25}O_2$ solid solution forms without CeO_2 or ZrO_2 segregation; and the characteristic peak derived from the Zr^{4+}-O-Ce^{4+} and Zr^{4+}-O-Zr^{4+} vibrations blue shifts to 607 cm^{-1} for the quick cooling sample compared with the annealed sample (599 cm^{-1}). This is attributed to the fact that the diverse Ce and Zr distribution at high temperature was retained due to the quick cooling, which leads to the higher ratio of Structure (d) in $Ce_{0.75}Zr_{0.25}O_2$ than the annealed sample. Therefore, the vibration signal of Zr^{4+}-O-Zr^{4+} in Raman spectrum increases, which leads to the blueshift and broadening of the characteristic peak at 580 ~ 630 cm^{-1}. For the samples annealed for 4 h, the structural stress is eliminated upon annealing and leads to a higher ratio of Structure (a). Hence its vibration peak of Zr^{4+}-O-Ce^{4+} is relatively high, which is well consistent with the theoretical deduction. Therefore, it is feasible to deduce the structural information of metal composite oxides by combining the experimental Raman spectra and simulated spectra.

To demonstrate the feasibility of the present method, rutile and anatase TiO_2 which have been widely applied in photocatalysis were adopted [45–48]; and their Raman spectra, as well as mixture (53.4 % rutile and 46.6 % anatase) were calculated and shown in Fig. 4. Fig. 4(a) shows that the Raman peaks of B_{1g}, E_g, A_{1g} and B_{2g} vibration modes are at 182, 462, 606 and 714 cm^{-1}, respectively, which are in good accordance with the experimental results. Meanwhile, as depicted in Fig. 4(b), the E_g peaks of anatase TiO_2 correspond to 168 and 642 cm^{-1}; the B_{1g} peaks are at 378 and 493 cm^{-1}; the A_{1g} peak is at 513 cm^{-1}, which also agree with experimental results [49].

On the basis of the experimental ratio of rutile (0.534) and anatase (0.466) TiO_2, the weighted Raman spectrum was calculated. Fig. 4(a) shows that the peak at 168 cm^{-1} is derived from the overlap of the B_{1g} mode of rutile and E_g mode of anatase TiO_2; the peaks at 350 ~ 550 cm^{-1} are contributed by the E_g, B_{1g} and A_{1g} modes of rutile and anatase TiO_2, respectively; the peaks at 606 and 642 cm^{-1} are attributed to the A_{1g} of rutile and E_g of anatase TiO_2, respectively. These results indicate that the weighted simulated Raman spectrum of TiO_2 mixture is well consistent with the experimental results [46]. Therefore, the practical spectrum of composite oxide is derived from the overlap of Raman spectra with different structures, and the weighted simulation Raman spectra can provide important structural information of metal composite oxides.

4. Conclusion

In summary, to solve the challenge of the microstructures of composite oxide, global structure optimization, structure proportion with temperature determined by Boltzmann distribution, and the weighted simulation Raman Spectrum was integrated. It follows the steps: (1) Optimization of the possible structures with different microstructures; (2) Calculation of the proportions of different structures by Boltzmann distribution law; (3) Simulation of Raman spectra of different structures by DFPT theory; (4) Computation of the weighted Raman spectrum on the basis of the proportion of different structures. Using $Ce_xZr_{1-x}O_2$ as a model, the microstructure of Ce and Zr distribution in $Ce_{1-x}Zr_xO_2$ solution at different temperature can be determined by combining with the experimental and simulated Raman spectra. It is further validated by rutile and anatase TiO_2 mixture. We anticipate that the present method provides an effective solution and a powerful tool for exploring the

Table 1
Free energy and population of the possible $Ce_6Zr_2O_{16}$ configurations.

Structure	Degeneracy	$G_{0\ K}$/eV mol^{-1}	Population at 0 K	$G_{300\ K}$ /eV mol^{-1}	Population at 300 K	$G_{773\ K}$ /eV mol^{-1}	Population at 773 K
(a)	4	−201.470	1.00	−201.809	0.279	−203.704	0.190
(b)	16	−201.455	0	−201.796	0.677	−203.693	0.646
(c)	4	−201.401	0	−201.744	0.023	−203.643	0.076
(d)	4	−201.388	0	−201.741	0.020	−203.652	0.088

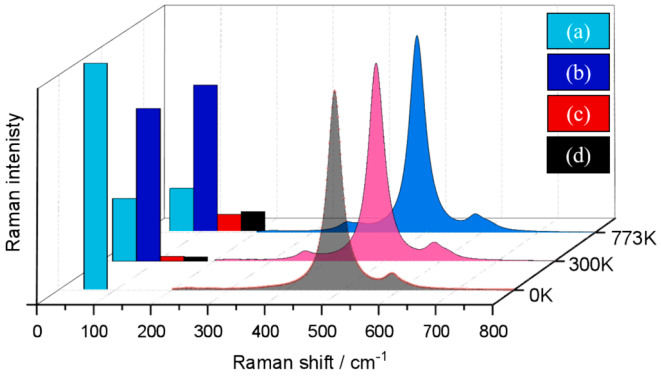

Fig. 2. Weighted Raman spectra at different temperatures.

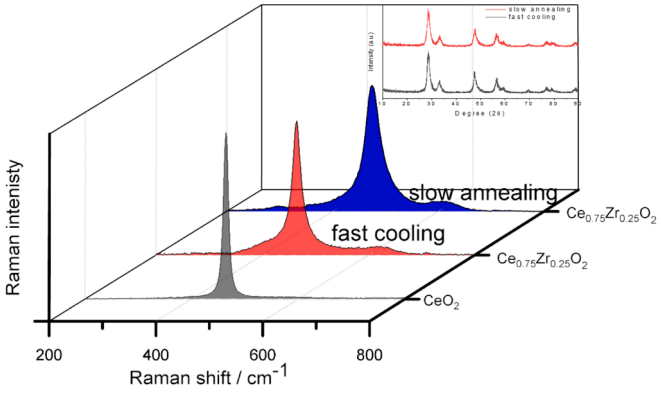

Fig. 3. Raman spectra of $Ce_{0.75}Zr_{0.25}O_2$ samples calcined at 773 K for 4 h. The inset is XRD patterns of $Ce_{0.75}Zr_{0.25}O_2$ solid solution with slow annealing (redline) and fast cooling (black line).

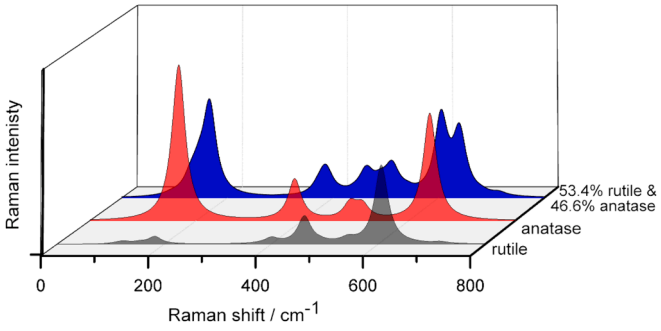

Fig. 4. Simulated Raman spectra of rutile (a) and anatase (b) TiO_2.

microstructure of composites.

CRediT authorship contribution statement

Le Liu: Writing – original draft, Investigation, Formal analysis. **Yuxing Xu:** Validation, Investigation, Funding acquisition. **Junchao Su:** Formal analysis. **Jiangtao Wei:** Formal analysis. **Xingchen Liu:** Writing – review & editing, Formal analysis. **Qing Peng:** Writing – review & editing, Formal analysis, Conceptualization. **Jie Chang:** Writing – review & editing, Formal analysis, Conceptualization. **Botao Teng:** Writing – review & editing, Supervision, Project administration, Funding acquisition, Conceptualization.

Declaration of competing interest

The authors declare that they have no known competing financial interests or personal relationships that could have appeared to influence the work reported in this paper.

Data availability

The data that support the findings of this study are available from the corresponding author upon reasonable request.

Acknowledgements

This work was supported by the National Natural Science Foundation of China (No. 22372120, 22372187, 21972160). B. Teng thanks the support by the Foundation of State Key Laboratory of Coal Conversion (Grant No. J21-22-908). Qing Peng thanks LiYing Program of the Institute of Mechanics, Chinese Academy of Sciences (E1Z1011001).

Appendix A. Supplementary data

Supplementary data to this article can be found online at https://doi.org/10.1016/j.saa.2024.124616.

References

[1] E.W. McFarland, H. Metiu, Catalysis by doped oxides, Chem. Rev. 113 (6) (2013) 4391–4427, https://doi.org/10.1021/cr300418s.
[2] D. García Pintos, A. Juan, B. Irigoyen, Mn-doped CeO_2: DFT+U study of a catalyst for oxidation reactions, J. Phys. Chem. C 117 (35) (2013) 18063–18073, https://doi.org/10.1021/jp403911b.
[3] J. Xu, G. Lu, Y. Guo, Y. Guo, X.-Q. Gong, A highly effective catalyst of Co-CeO_2 for the oxidation of diesel soot: the excellent NO oxidation activity and NO_x storage capacity, Appl. Catal., A 535 (2017) 1–8, https://doi.org/10.1016/j.apcata.2017.02.005.
[4] P.G. Lustemberg, Z. Mao, A. Salcedo, B. Irigoyen, M.V. Ganduglia-Pirovano, C. T. Campbell, Nature of the active sites on Ni/CeO_2 catalysts for methane conversions, ACS Catal. 11 (16) (2021) 10604–10613, https://doi.org/10.1021/acscatal.1c02154.
[5] J. Wang, X.-Q. Gong, A DFT + U study of V, Cr and Mn doped CeO_2(111), Appl. Surf. Sci. 428 (2018) 377–384, https://doi.org/10.1016/j.apsusc.2017.09.120.
[6] Y. Yang, Y. Zhuang, Y. He, B. Bai, X. Wang, Fine tuning of the dimensionality of zinc silicate nanostructures and their application as highly efficient absorbents for toxic metal ions, Nano Res. 3 (8) (2010) 581–593, https://doi.org/10.1007/s12274-010-0019-3.
[7] X. Xu, X. Wang, Fine tuning of the sizes and phases of ZrO_2 nanocrystals, Nano Res. 2 (11) (2009) 891–902, https://doi.org/10.1007/s12274-009-9092-x.
[8] D. Hua-Qing, P.A.N. Xi, X.I.E. Qin, M. Qiang-Qiang, G.A.O. Jian-Rong, W. Jian-Guo, CO Adsorption and oxidation on metal-doped TiO_2 nanotube arrays, Acta Phys. Chim. Sin. 28 (01) (2012) 44–50, https://doi.org/10.3866/pku.Whxb20122844.
[9] D. Li, K. Li, R. Xu, H. Wang, D. Tian, Y. Wei, X. Zhu, C. Zeng, L. Zeng, $Ce_{1-x}Fe_xO_{2-\delta}$ catalysts for catalytic methane combustion: role of oxygen vacancy and structural dependence, Catal. Today 318 (2018) 73–85, https://doi.org/10.1016/j.cattod.2017.12.015.
[10] E. Sartoretti, C. Novara, F. Giorgis, M. Piumetti, S. Bensaid, N. Russo, D. Fino, In situ Raman analyses of the soot oxidation reaction over nanostructured ceria-based

catalysts, Sci. Rep. 9 (1) (2019) 3875, https://doi.org/10.1038/s41598-019-39105-5.
[11] J. Yu, Z. Si, L. Chen, X. Wu, D. Weng, Selective catalytic reduction of NO by ammonia over phosphate-containing $Ce_{0.75}Zr_{0.25}O_2$ solids, Appl. Catal., B 163 (2015) 223–232, https://doi.org/10.1016/j.apcatb.2014.08.006.
[12] N.B. Saleh, D.J. Milliron, N. Aich, L.E. Katz, H.M. Liljestrand, M.J. Kirisits, Importance of doping, dopant distribution, and defects on electronic band structure alteration of metal oxide nanoparticles: Implications for reactive oxygen species, Sci. Total Environ. 568 (2016) 926–932, https://doi.org/10.1016/j.scitotenv.2016.06.145.
[13] Y. Zhao, B.-T. Teng, X.-D. Wen, Y. Zhao, L.-H. Zhao, M.-F. Luo, A theoretical evaluation and comparison of $M_xCe_{1-x}O_{2-\delta}$ (M = Au, Pd, Pt, and Rh) catalysts, Catal. Commun. 27 (2012) 63–68, https://doi.org/10.1016/j.catcom.2012.06.027.
[14] Y. Zhao, B.-T. Teng, X.-D. Wen, Y. Zhao, Q.-P. Chen, L.-H. Zhao, M.-F. Luo, Superoxide and peroxide species on CeO_2(111), and their oxidation roles, J. Phys. Chem. C 116 (30) (2012) 15986–15991, https://doi.org/10.1021/jp3016326.
[15] B.-T. Teng, J.-J. Lang, X.-D. Wen, C. Zhang, M. Fan, H.G. Harris, O_2 Adsorption and oxidative activity on gold-based catalysts with and without a ceria support, J. Phys. Chem. C 117 (37) (2013) 18986–18993, https://doi.org/10.1021/jp4056279.
[16] T. Montini, M. Melchionna, M. Monai, P. Fornasiero, Fundamentals and catalytic applications of CeO_2-based materials, Chem. Rev. 116 (10) (2016) 5987–6041, https://doi.org/10.1021/acs.chemrev.5b00603.
[17] D. Zhang, J. Yang, Q. Jiang, Z. Zhou, X. Li, J. Xin, A. Basit, Y. Ren, X. He, Multi-cations compound Cu_2CoSnS_4: DFT calculating, band engineering and thermoelectric performance regulation, Nano Energy 36 (2017) 156–165, https://doi.org/10.1016/j.nanoen.2017.04.027.
[18] J. Dai, Z. Gong, S. Xu, Y. Cui, M. Yao, In situ study on the initial oxidation behavior of zirconium alloys with near-ambient pressure XPS, Acta Phys. Chim. Sin. 38 (3) (2020) 2003026, https://doi.org/10.3866/pku.Whxb202003026.
[19] G.A. Somorjai, Y. Li, Introduction to surface chemistry and catalysis, John Wiley & Sons, 2010.
[20] R.S. Das, Y.K. Agrawal, Raman spectroscopy: Recent advancements, techniques and applications, Vib. Spectrosc. 57 (2) (2011) 163–176, https://doi.org/10.1016/j.vibspec.2011.08.003.
[21] J. Krajczewski, A. Kudelski, Shell-isolated nanoparticle-enhanced raman spectroscopy, Front. Chem. 7 (2019) 410, https://doi.org/10.3389/fchem.2019.00410.
[22] T. Touzalin, S. Joiret, E. Maisonhaute, I.T. Lucas, Complex electron transfer pathway at a microelectrode captured by in situ nanospectroscopy, Anal. Chem. 89 (17) (2017) 8974–8980, https://doi.org/10.1021/acs.analchem.7b01542.
[23] Y. Fang, J.C. Dong, S.Y. Ding, J. Cheng, J.M. Feliu, J.F. Li, Z.Q. Tian, Toward a quantitative theoretical method for infrared and Raman spectroscopic studies on single-crystal electrode/liquid interfaces, Chem. Sci. 11 (5) (2019) 1425–1430, https://doi.org/10.1039/c9sc05429d.
[24] T. Touzalin, S. Joiret, E. Maisonhaute, I.T. Lucas, Capturing electrochemical transformations by tip-enhanced Raman spectroscopy, Curr. Opin. Electrochem. 6 (1) (2017) 46–52, https://doi.org/10.1016/j.coelec.2017.10.016.
[25] T. Touzalin, S. Joiret, I.T. Lucas, E. Maisonhaute, Electrochemical tip-enhanced Raman spectroscopy imaging with 8 nm lateral resolution, Electrochem. Commun. 108 (2019) 106557, https://doi.org/10.1016/j.elecom.2019.106557.
[26] C. Hess, New advances in using Raman spectroscopy for the characterization of catalysts and catalytic reactions, Chem. Soc. Rev. 50 (5) (2021) 3519–3564, https://doi.org/10.1039/d0cs01059f.
[27] L. Li, F. Chen, J.Q. Lu, M.F. Luo, Study of defect sites in $Ce_{1-x}M_xO_{2-\delta}$ (x = 0.2) solid solutions using Raman spectroscopy, J. Phys. Chem. A 115 (27) (2011) 7972–7977, https://doi.org/10.1021/jp203921m.
[28] Y. Xu, F. Wang, X. Liu, Y. Liu, M. Luo, B. Teng, M. Fan, X. Liu, Resolving a Decade-Long Question of Oxygen Defects in Raman Spectra of Ceria-Based Catalysts at Atomic Level, J. Phys. Chem. C 123 (31) (2019) 18889–18894, https://doi.org/10.1021/acs.jpcc.9b00633.
[29] K. Yang, C. Oses, S. Curtarolo, Modeling Off-Stoichiometry Materials with a High-Throughput Ab-Initio Approach, Chem. Mater. 28 (18) (2016) 6484–6492, https://doi.org/10.1021/acs.chemmater.6b01449.
[30] R.F. Moran, D. McKay, P.C. Tornstrom, A. Aziz, A. Fernandes, R. Grau-Crespo, S. E. Ashbrook, Ensemble-based modeling of the NMR spectra of solid solutions: cation disorder in Y2(Sn, Ti)2O7, J. Am. Chem. Soc. 141 (44) (2019) 17838–17846, https://doi.org/10.1021/jacs.9b09036.
[31] J.J. Plata, A.M. Márquez, S. Cuesta-López, J.F. Sanz, Connecting experimental synthetic variables with the microstructure and electronic properties of doped ferroelectric perovskites for solar cell applications using high-throughput frameworks, Acta Mater. 204 (2021) 116466, https://doi.org/10.1016/j.actamat.2020.11.008.
[32] Q. Yuan, Q. Liu, W.-G. Song, W. Feng, W.-L. Pu, L.-D. Sun, Y.-W. Zhang, C.-H. Yan, Ordered mesoporous $Ce_{1-x}Zr_xO_2$ solid solutions with crystalline walls, J. Am. Chem. Soc. 129 (21) (2007) 6698–6699, https://doi.org/10.1021/ja070908q.
[33] F. Cova, D.G. Pintos, A. Juan, B. Irigoyen, A first-principles modeling of ni interactions on CeO_2−ZrO_2 mixed oxide solid solutions, J. Phys. Chem. C 115 (15) (2011) 7456–7465, https://doi.org/10.1021/jp1108703.
[34] R. Grau-Crespo, S. Hamad, C.R.A. Catlow, N.H.D. Leeuw, Symmetry-adapted configurational modelling of fractional site occupancy in solids, J. Phys.: Condens. Matter 19 (25) (2007) 256201, https://doi.org/10.1088/0953-8984/19/25/256201.
[35] G. Kresse, J. Furthmüller, Efficient iterative schemes for ab initio total-energy calculations using a plane-wave basis set, Phys. Rev. B 54 (16) (1996) 11169, https://doi.org/10.1103/PhysRevB.54.11169.
[36] P.E. Blochl, Projector augmented-wave method, Phys. Rev. B 50 (24) (1994) 17953–17979, https://doi.org/10.1103/physrevb.50.17953.
[37] J.P. Perdew, K. Burke, M. Ernzerhof, Generalized gradient approximation made simple, Phys. Rev. Lett. 77 (18) (1996) 3865, https://doi.org/10.1103/PhysRevLett.77.3865.
[38] H.J. Monkhorst, J.D. Pack, Special points for Brillouin-zone integrations, Phys. Rev. B 13 (12) (1976) 5188–5192, https://doi.org/10.1103/PhysRevB.13.5188.
[39] X.-Q. Gong, L.-L. Yin, J. Zhang, H.-F. Wang, X.-M. Cao, G. Lu, P. Hu, Computational Simulation of Rare Earth Catalysis, Catal. Kinetics – Mol. Level Considerations, Adv. Chem. Eng. 44 (2014) 1–60, https://doi.org/10.1016/b978-0-12-419974-3.
[40] X.P. Wu, X.Q. Gong, Unique electronic and structural effects in vanadia/ceria-catalyzed reactions, J. Am. Chem. Soc. 137 (41) (2015) 13228–13231, https://doi.org/10.1021/jacs.5b07939.
[41] X. Gonze, D.C. Allan, M.P. Teter, Dielectric tensor, effective charges, and phonons in alpha -quartz by variational density-functional perturbation theory, Phys. Rev. Lett. 68 (24) (1992) 3603–3606, https://doi.org/10.1103/PhysRevLett.68.3603.
[42] S. Baroni, S. De Gironcoli, A. Dal Corso, P. Giannozzi, Phonons and related crystal properties from density-functional perturbation theory, Rev. Mod. Phys. 73 (2) (2001) 515, https://doi.org/10.1103/RevModPhys.73.515.
[43] X. Gonze, C. Lee, Dynamical matrices, Born effective charges, dielectric permittivity tensors, and interatomic force constants from density-functional perturbation theory, Phys. Rev. B 55 (16) (1997) 10355, https://doi.org/10.1103/PhysRevB.55.10355.
[44] S. Trasatti, Electrochim, Acta 52 (7) (2007) 2729–2730, https://doi.org/10.1016/j.electacta.2006.09.003.
[45] S.D. Mo, W.Y. Ching, Electronic and optical properties of three phases of titanium dioxide: Rutile, anatase, and brookite, Phys. Rev. B 51 (19) (1995) 13023–13032, https://doi.org/10.1103/physrevb.51.13023.
[46] A.R. Zanatta, A fast-reliable methodology to estimate the concentration of rutile or anatase phases of TiO_2, AIP Adv. 7 (7) (2017) 075201, https://doi.org/10.1063/1.4992130.
[47] J. Sanz, J. Soria, I. Sobrados, S. Yurdakal, V. Augugliaro, Influence of Amorphous TiO_{2-x} on Titania Nanoparticle Growth and Anatase-to-Rutile Transformation, J. Phys. Chem. C 116 (8) (2012) 5110–5115, https://doi.org/10.1021/jp2112044.
[48] W. Lun-Peng, Z. Lian-Hua, Z. Hai-Ming, Z. Qing-Nan, Effects of the adsorption of oxygen on the photocatalytic activity of TiO_2 films using photocurrent method, Acta Phys. Chim. Sin. 23 (5) (2007) 765–768, https://doi.org/10.3866/PKU.WHXB20070528.
[49] H. Ma, G. Guo, J. Yang, Y. Guo, N. Ma, Femtosecond laser irradiation-induced phase transformation on titanium dioxide crystal surface, Nucl. Instrum. Methods Phys. Res., Sect. B 264 (1) (2007) 61–65, https://doi.org/10.1016/j.nimb.2007.08.006.